J Solid State Electrochem (2017) 21:3301–3314
DOI 10.1007/s10008-017-3655-7

ORIGINAL PAPER

Relationship between the crystal structures of $LiMn_{1.5}Ni_{0.5}O_4$ and $LiMn_{1.5}Ni_{0.45}Fe_{0.05}O_4$ and their internal resistances as cathode materials for lithium ion batteries

Ryosuke Okamoto[1] · **Kazuhide Hayashi**[2] · **Satoshi Matsumoto**[2] · **Naomi Suzuki**[2] · **Masami Terauchi**[3]

Received: 20 January 2017 / Revised: 10 May 2017 / Accepted: 17 May 2017 / Published online: 24 June 2017

Abstract It has been reported that the partial substitution of Fe for Ni in $LiMn_{1.5}Ni_{0.5}O_4$ improves the rate capability of batteries wherein it is used as a cathode material. To understand the mechanism of this improvement, $LiMn_{1.5}Ni_{0.5}O_4$ and $LiMn_{1.5}Ni_{0.45}Fe_{0.05}O_4$ samples were prepared to compare their crystal structures and the internal resistances of batteries fabricated using them. Electrochemical measurements showed that resistance of $LiMn_{1.5}Ni_{0.45}Fe_{0.05}O_4$ to the diffusion of Li^+ ions into bulk is lower than that for $LiMn_{1.5}Ni_{0.5}O_4$. The crystal structures of $LiMn_{1.5}Ni_{0.5}O_4$ and $LiMn_{1.5}Ni_{0.45}Fe_{0.05}O_4$ were examined by neutron diffraction and transmission electron microscopy. The mass percentage of the ordered $P4_332$ phase in $LiMn_{1.5}Ni_{0.45}Fe_{0.05}O_4$ was found to be smaller than that in $LiMn_{1.5}Ni_{0.5}O_4$, and the coexistence of an ordered $P4_332$ phase and a disordered $Fd\bar{3}m$ phase leads to the formation of boundaries in the primary particles of the samples. From these results, it was proposed that the reason for the internal resistance improvement was that the boundaries between the $P4_332$ and $Fd\bar{3}m$ phase impeded the diffusion of Li^+ ions. Therefore, $LiMn_{1.5}Ni_{0.45}Fe_{0.05}O_4$ exhibited lower internal resistance because it contained a lower amount of $P4_332$ phase and consequently, a lower occurrence of boundaries.

✉ Ryosuke Okamoto
Ryosuke_Okamoto@ni.smm.co.jp

[1] Battery Research Laboratories, Sumitomo Metal Mining Co., Ltd, 17-3 Isoura-cho, Niihama, Ehime 792-0002, Japan

[2] Ichikawa Research Center, Sumitomo Metal Mining Co., Ltd, 18-5, Nakakokubun 3-chome, Ichikawa, Chiba 272-8588, Japan

[3] Institute of Multidisciplinary Research for Advanced Materials, Tohoku University, 2-1-1 Katahira Aoba-ku, Sendai, Miyagi 980-8577, Japan

Keywords High-voltage cathode material · Cation ordering · Neutron diffraction · Transmission electron microscopy · Dark-field image · Diffusion of Li^+ ions

Introduction

The applications of secondary lithium batteries have expanded from portable electronic devices to electric vehicles, leading to considerable research attention being paid to increasing their energy density. High battery voltage is an important goal in the development of high-energy-density batteries. Various cathode materials with spinel-type crystallographic structures, i.e., $LiMn_{2-x}M_xO_4$ (M = Cr, Fe, Co, Ni, or Cu), have been developed for high-voltage operations [1–5]. $LiMn_{1.5}Ni_{0.5}O_4$ is a promising cathode material because it exhibits a large (>130 mAh/g) charge/discharge plateau in the high-potential region around 4.7 V (vs. Li^+/Li) [4]. Alcántara et al. have reported that partial substitution of Fe for Ni in $LiMn_{1.5}Ni_{0.5}O_4$ (subsequently referred to as Fe substitution) leads to high capacities and excellent cycle durability [6]. The authors explained that this excellent cycle durability was due to homogeneous Li insertion/extraction without crystal phase separation. Liu et al. have reported that a high rate capability is also conferred by Fe substitution [7]. Several hypotheses have been proposed to explain this improvement in rate capability. The major hypotheses are as follows: (1) stabilization of the cation-disordered octahedral sites in the spinel structure and (2) production of Mn^{3+} ions and consequent enhancement of electronic conductivity. These hypotheses are summarized below.

1) Stabilization of the cation-disordered octahedral sites in the spinel structure: There are two different crystallographic structures for $LiMn_{1.5}Ni_{0.5}O_4$ [8] and they are

classified into the space groups $Fd\bar{3}m$ and $P4_332$. The Mn and Ni ions in the spinel structure occupy the octahedral sites in a face-centered cubic (FCC) lattice composed of oxygen ions. The Mn and Ni ions occupy the octahedral sites randomly in $LiMn_{1.5}Ni_{0.5}O_4$ with the space group $Fd\bar{3}m$, whereas they are regularly ordered in $LiMn_{1.5}Ni_{0.5}O_4$ with the space group $P4_332$. Kim et al. have reported that Li ion extraction from the ordered $LiMn_{1.5}Ni_{0.5}O_4$ leads to the disordering of Mn and Ni ions and phase transition from $P4_332$ to $Fd\bar{3}m$ [9, 10]. Liu et al. showed that Fe substitution stabilizes the disordered $Fd\bar{3}m$ phase and suppresses the formation of the ordered phase [7].

2) Production of Mn^{3+} ions and consequent enhancement of electronic conductivity: In $LiMn_{1.5}Ni_{0.5}O_4$, the substitution of Fe^{3+} ions for Ni^{2+} ions reduces tetravalent Mn ions to trivalent Mn ions in order to maintain electronic neutrality. The coexistence of Mn^{3+} and Mn^{4+} ions in the solid causes an enhancement of electronic conductivity owing to electron hopping between Mn^{3+} and Mn^{4+} sites, and thereby increases the rate of the accompanying Li^+ ion migration [11].

The aim of this study was to investigate the mechanism to improve the rate capability of $LiMn_{1.5}Ni_{0.5}O_4$ by Fe substitution. $LiMn_{1.5}Ni_{0.5}O_4$ and $LiMn_{1.5}Ni_{0.45}Fe_{0.05}O_4$ samples were synthesized to compare their as-synthesized or delithiated crystal structures and the internal resistances of the batteries using these samples as cathode materials, at several states of charge. According to previous studies, the ordering of Mn and Ni ions plays an important role in this improvement. Neutron powder diffraction (ND) and Rietveld refinement of the diffraction data were used to quantify the amounts of $P4_332$ phase in the samples, whereas dark-field imaging by transmission electron microscopy (TEM) was used to visualize the distributions of the $P4_332$ phase in the samples.

Experimental

$LiMn_{1.5}Ni_{0.5}O_4$ and $LiMn_{1.5}Ni_{0.45}Fe_{0.05}O_4$ samples were synthesized using a hydroxide precursor method. The hydroxide precursors were precipitated from a solution containing the required quantities of manganese, nickel, and iron sulfate by adding NaOH. The mixture of precursors and the required amount of Li_2CO_3 was heated at 900 °C for 12 h and then 700 °C for 18 h under flowing air.

The surface areas of the samples were measured by the Brunauer–Emmett–Teller (BET) absorption method (Macsorb, MOUNTECH). To measure the tap densities, about 8 g of samples were placed in 20-ml graduated cylinders and tapped 500 times by a tap density analyzer (TPM-1P, Tsutsui Scientific Instruments). The morphologies of the samples were observed by scanning electron microscopy (SEM; JSM-7001F, JEOL). Time-of-flight ND patterns were recorded on a neutron diffractometer (iMATERIA; BL20, MLF, J-PARC). The sample was placed in a vanadium tube and mounted within an evacuated furnace. The data collected on the backscattering detector bank were subjected to Rietveld refinement using the Z-Rietveld code. Electron diffraction (ED) patterns and electron microscopy images were obtained using a transmission electron microscope (JEM 2000ES, JEOL) operated at 100 kV.

Electrochemical measurements and the preparation of delithiated samples were performed using CR2032 coin-type cells. To prepare the cathodes, 85 wt% active material, 10 wt% acetylene black, and 5 wt% polyvinylidene difluoride (PVDF) binder were mixed in *N*-methyl-2-pyrrolidone solvent. The mixture was placed on thin aluminum sheets and then dried in an oven at 100 °C. The cathode material-loaded sheets were pressed by a roll press machine and then cut into circular electrodes with an area of 1.33 cm^2. On average, the cathodes had an active material content of 5 mg/cm^2. The coin cells were fabricated using cathodes, metallic lithium anodes, 1 M $LiPF_6$ in dimethyl carbonate/ethylene carbonate electrolyte (1:1 *w/w*), and a glass fiber separator.

The cathodes for ex situ ND were prepared by mixing 70 wt% active material and 30 wt% conductive binder (35 wt% polytetrafluoroethylene and 65 wt% acetylene black) without a solvent. The mixture was pressed on a 1.54-cm^2 stainless steel mesh that was used as a current collector. Initial charge/discharge performances were measured within the voltage range of 3.0–5.0 V at a constant C-rate of 0.05 C at 25 °C using a HJ1005SD8 battery charge/discharge system (HOKUTO DENKO). The C-rate was calculated on the basis of 1 C = 148 mA/g. The second charge/discharge capacities were regarded as fully charged/discharged because the first charge/discharge involved the irreversible capacity corresponding to the decomposition of electrolyte. This electrolyte decomposition was caused by the high-voltage charging over the potential window of the electrolyte. The direct current (DC) resistance and the impedance measurements were performed with batteries charged to a given state-of-charge (SOC), which is represented as the percentage of a certain capacity to the fully charged capacity. For DC resistance measurements, the charged batteries were left to stand for 1 min and then discharged for 10 s at a constant C-rate of 1/3 C, 1 C, 2 C, or 5 C. The voltage drop resulting from the momentary discharge was recorded. The DC resistance is represented as the slope calculated for the linear relationship between the current and the voltage drop. Impedance measurements were collected with an alternating current (AC) amplitude of 10 mV in the frequency range of 100 kHz–0.1 Hz using a VSP-300 multi-potentiostat (Biologic).

For the cycling test, Al-laminate-type batteries containing a 3.0 × 5.0 cm^2 cathode with a carbon composite anode were used. The carbon composite anode comprised 90 wt% graphite, 10 wt% PVDF, and a Cu foil as a current collector. The batteries were charged and discharged for 5 cycles at a constant C-rate of 1/4 C before cycling tested to form a solid–electrolyte interface (SEI) on the anode surface. The cycling test was performed for 200 cycles of charge/discharge at a constant C-rate of 2 C at 60 °C. After the cycling tests, the amount of Mn and Ni on the anodes retrieved from the disassembled batteries was measured by inductively coupled plasma–optical emission spectrometry (ICP–OES; 725-ES, Varian).

In situ X-ray diffraction (XRD) was performed with a D8 DISCOVER X-ray diffractometer (BRUKER) using monochromated CuKα radiation between 13° and 45° at a scan rate of 0.01°/s. Al-laminate-type batteries containing a 3.0 × 5.0 cm^2 cathode with a Li-foil anode were used for in situ XRD. The laminate-type batteries were fabricated in a similar manner as those used for electrochemical performance measurements. Charge/discharge was performed in the voltage range of 3.0–5.0 V at a constant C-rate of 0.03 C at 25 °C.

The ab initio calculations based on density functional theory (DFT) [12] were performed using the Vienna ab initio simulation package (VASP) [13–16]. The calculations were performed using the Perdew–Burke–Ernzerhof (PBE) exchange-correlation functional [17], which is a generalized gradient approximation (GGA) method [18]. A projector augmented wave (PAW) scheme was used to treat the core electrons [19]. The spin-polarized magnetic calculations were conducted using a plane-wave cutoff energy of 648 eV and k-spacing of a 2 × 2 × 2 mesh. The +U correction term was used with U = 5.00 for Ni 3d, Mn 3d, and Fe 3d [20]. The crystal structure model was based on a previous report [21]. A single cubic unit cell with lattice constant a = 8.170 Å and chemical composition $Li_8Mn_{12}Ni_{4-y}Fe_yO_{32}$ (y = 0 or 1) was used for the calculation. For structure optimization, the atom positions, unit cell shape, and unit cell volume were fully relaxed to minimize the total energy.

Results and discussion

Characterization of the prepared samples

As shown in Table 1, the BET surface areas of $LiMn_{1.5}Ni_{0.5}O_4$ and $LiMn_{1.5}Ni_{0.45}Fe_{0.05}O_4$ are the same. This is consistent with the SEM observations. The SEM images of both samples, as shown in Fig. 1, present the same morphology. Octahedral primary particles of ca. 500-nm diameter aggregate and form semi-spherical secondary particles of ca. 5-μm diameter. These observations prove that the morphology of the cathode materials does not influence the internal resistance of their batteries. For instance, the contribution of the diffusion distance of Li^+ ions for the resistance can be neglected, as will be described in the subsequent section.

Figure 2 shows the ND patterns of the as-synthesized $LiMn_{1.5}Ni_{0.5}O_4$ and $LiMn_{1.5}Ni_{0.45}Fe_{0.05}O_4$. These patterns are normalized by the maximum peak intensity of the (222) peak at ca. 2.36 Å, which has the strongest intensity in each pattern. The ND patterns exhibit two types of peaks attributed to the $Fd\bar{3}m$ and $P4_332$ space groups. These peaks are denoted as F and P peaks, respectively. The peak at 2.08 Å is due to $Li_xNi_{1-x}O$ or Mn–Ni oxide impurity phases, which are produced by calcination above ca. 700 °C and consequent oxygen loss [22]. The intensity of the P peaks (indicated by the + symbol) for $LiMn_{1.5}Ni_{0.5}O_4$ is stronger than that for $LiMn_{1.5}Ni_{0.45}Fe_{0.05}O_4$, although the F peaks (without the + symbol) exhibit the same intensity for both samples. Furthermore, the full-width-at-half-maximum (FWHM) values of the P peaks are larger than those of the F peaks. This indicates that the volume fractions of the $P4_332$ and $Fd\bar{3}m$ phases and the crystallinities are different in the as-synthesized $LiMn_{1.5}Ni_{0.5}O_4$ and $LiMn_{1.5}Ni_{0.45}Fe_{0.05}O_4$ samples. Rietveld refinement was performed to determine the quantities of each phase in the samples. The refined results for the mass percentages of the $P4_332$ and $Fd\bar{3}m$ phases and the lattice constant a, which is the only parameter for a cubic unit cell, are listed in Table 2. The mass percentage of the $P4_332$ phase is larger than that of the $Fd\bar{3}m$ phase in $LiMn_{1.5}Ni_{0.5}O_4$. In contrast, the $Fd\bar{3}m$ phase dominates in $LiMn_{1.5}Ni_{0.45}Fe_{0.05}O_4$. This result confirms that Fe substitution stabilizes the disordered $Fd\bar{3}m$ phase, as reported by Liu et al. [7]. The lattice constants for the $P4_332$ phases of both samples are almost the same. However, the lattice constant of the $Fd\bar{3}m$ phase in $LiMn_{1.5}Ni_{0.45}Fe_{0.05}O_4$ is larger than that in $LiMn_{1.5}Ni_{0.5}O_4$. The larger lattice constant in $LiMn_{1.5}Ni_{0.45}Fe_{0.05}O_4$ is due to the production of Mn^{3+} ions upon Fe substitution. The larger ionic radius of Mn^{3+} (0.79 Å) compared to that of Mn^{4+} (0.67 Å) leads to an increase in the volume of the unit cell. The similarity of the lattice constants of the $P4_332$ phases in the two samples suggests that Mn^{3+} ions and the accompanying Fe^{3+} ions are not contained in the $P4_332$ phase of $LiMn_{1.5}Ni_{0.45}Fe_{0.05}O_4$ and they occupy the octahedral sites of the $Fd\bar{3}m$ phase.

As shown in Fig. 3a, the selected area ED pattern of the ordered $P4_332$ phase in $LiMn_{1.5}Ni_{0.5}O_4$ presents extra spots, for example, $\bar{1}$ 10, $\bar{1}$ $1\bar{2}$, and $2\bar{2}$ 1, which are forbidden for a spinel structure with the $Fd\bar{3}m$ space group. Figure 3b shows the dark-field image due to $\bar{1}$ 10 reflections, which is attributed to the $P4_332$ phase. This image was taken by exciting the $\bar{1}$ 10 spot under $\bar{h}$ h0 systematic excitation conditions. Many bright domains, separated by dark lines, and some dark domains are seen in Fig. 3b. The bright and dark domains are assigned to $P4_332$ and $Fd\bar{3}m$ phases, respectively. The dark lines can be assigned to

Table 1 BET surface area, tap density, and capacities of $LiMn_{1.5}Ni_{0.5}O_4$ and $LiMn_{1.5}Ni_{0.45}Fe_{0.05}O_4$

Sample	BET surface area	Tap density	Capacity	
			Charge	Discharge
	m^2/g	g/cm^3	mAh/g	
$LiMn_{1.5}Ni_{0.5}O_4$	1.1	1.2	140	136
$LiMn_{1.5}Ni_{0.45}Fe_{0.05}O_4$	1.1	1.4	142	137

anti-phase domain boundaries with a phase shift of a half of 110 lattice spacing. This image reveals that the ordering of Mn and Ni leads to the formation of domains in the primary particles of $LiMn_{1.5}Ni_{0.5}O_4$. The dark-field image due to the $\bar{2}$ 20 reflection for the same area was also recorded (Fig. 3c). As a $\bar{2}$ 20 reflection is allowed for both $Fd\bar{3}m$ and $P4_332$ phases, the dark lines and dark bands shown in Fig. 3b are not shown in Fig. 3c. The $Fd\bar{3}m$ and $P4_332$ phases contain different arrangements of transition metal elements; however, their oxygen atom arrangements are the same, forming a closed packing FCC lattice. Thus, the dark-field images indicate that the ordering of Mn and Ni ions forms domains regardless of the continuous FCC lattice. The smaller size of the bright domain observed in the dark-field image due to the $\bar{1}$ 10 reflection than that due to the $\bar{2}$ 20 reflection corresponds with the larger FWHM of the P peaks than that of the F peaks in the ND patterns (see Fig. 2) [23]. The same experiment was performed with the $LiMn_{1.5}Ni_{0.45}Fe_{0.05}O_4$ sample. However, extra spots due to the $P4_332$ phase were not observed. This seems to be inconsistent with the Rietveld refinement analysis of the ND data, which indicated that 17 wt% of the $P4_332$ phase existed in $LiMn_{1.5}Ni_{0.45}Fe_{0.05}O_4$. This discrepancy may be due to the smaller weight percent of the $P4_332$ phase and differences in the microscopic (TEM) and macroscopic (ND) methods. TEM can only examine a thin specimen region with a thickness smaller than 100 nm under the usual accelerating voltage conditions. In contrast, ND has a penetration depth of several centimeters and provides averaged information on specimens on the gram scale. Thus, it is possible that the $P4_332$ phase was undetected, but exists and forms domains within the $LiMn_{1.5}Ni_{0.45}Fe_{0.05}O_4$ sample.

Ab initio calculations of crystal structure stabilities

To reveal the mechanism for stabilization of the disordered $Fd\bar{3}m$ phase by Fe substitution, an ab initio calculation approach was adopted. If there were no lattice energy contributions, the Ni and Mn ions in $LiMn_{1.5}Ni_{0.5}O_4$ would randomly occupy the transition metal (TM) sites to increase the entropy of this crystal system. Therefore, the energy of the ordered $LiMn_{1.5}Ni_{0.5}O_4$ ($P4_332$ space group) is inevitably lower than that of the disordered $LiMn_{1.5}Ni_{0.5}O_4$ ($Fd\bar{3}m$ space group). To calculate and compare the energies of both structures, it was necessary to determine the structure of the disordered $LiMn_{1.5}Ni_{0.5}O_4$. However, the disordered $LiMn_{1.5}Ni_{0.5}O_4$ provides many possible configurations for the Mn and Ni ions. Figure 4a shows the crystal structure model of the ordered $LiMn_{1.5}Ni_{0.5}O_4$ (P model). Li^+ ions are excluded in Fig. 4 to better visualize the order of Mn and Ni ions. A unit cell of $LiMn_{1.5}Ni_{0.5}O_4$ has eight distorted-cube-shaped subunits composed of four TM ions and four oxygen ions, ignoring the double count of a Ni ion shared by two subunits. Each subunit in the P model has only one Ni ion. Figure 4b, c shows two variations of disordered $LiMn_{1.5}Ni_{0.5}O_4$ (A model and B model) that have the same lattice constant a and position of atoms with the P model but have different Mn and Ni ordering from the P model. The A model has four subunits occupied by two Ni ions and four subunits unoccupied by Ni ions. The B model has one subunit occupied by four Ni ions, three subunits unoccupied by Ni ions, and four subunits occupied by one Ni ion. Table 3 shows the minimized energies obtained from structure optimization of the P, A, and B models. Among

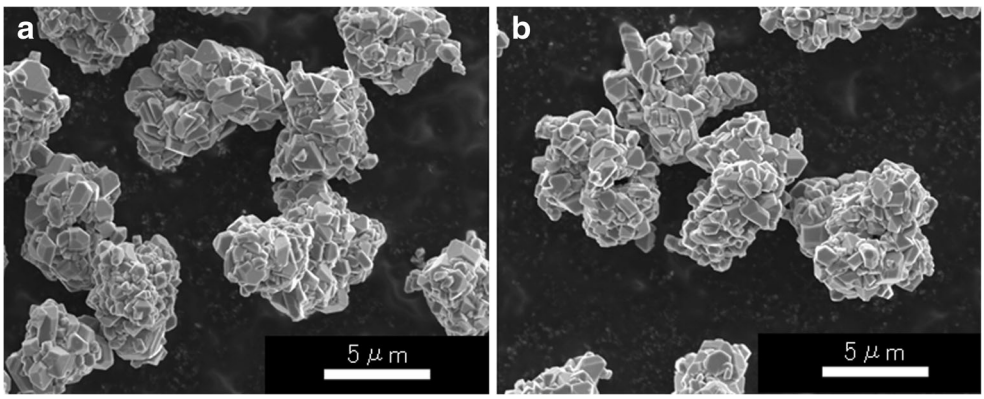

Fig. 1 SEM images of $LiMn_{1.5}Ni_{0.5}O_4$ (**a**) and $LiMn_{1.5}Ni_{0.45}Fe_{0.05}O_4$ (**b**)

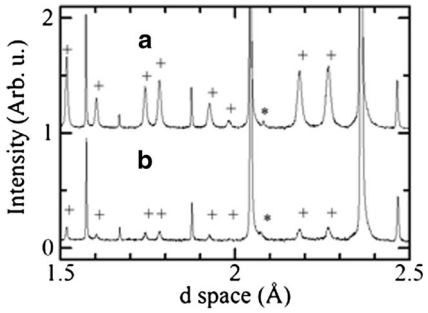

Fig. 2 ND patterns obtained from the as-synthesized samples: $LiMn_{1.5}Ni_{0.5}O_4$ (*a*) and $LiMn_{1.5}Ni_{0.45}Fe_{0.05}O_4$ (*b*). The peaks marked with *plus sign* are P peaks. The peak marked with *asterisk* is attributed to a $Li_xNi_{1-x}O$ impurity phase. The peaks without marks are F peaks

all the structures, the P model had the lowest energy, which demonstrates that the ordering of the Mn and Ni ions results from avoiding the formation of a subunit that has more than two Ni ions. The optimized energies of the P model, A model, and B model (in which one Fe ion is substituted for one Ni ion) are also listed in Table 3. The difference in energies between the Fe substituted P model and Fe substituted A model or B model is lower than that between non-substituted P model and non-substituted A model or B model. These results indicate that Fe substitution stabilizes the subunit that has more than two Ni ions. Consequently, this promotes disordering of the Mn and Ni ions.

Electrochemical performances

Table 1 shows the charge/discharge capacities of $LiMn_{1.5}Ni_{0.5}O_4$ and $LiMn_{1.5}Ni_{0.45}Fe_{0.05}O_4$ samples at the second cycle. Both samples have high reversible capacities close to the theoretical ones (148 mAh/g). Since the charge capacity of $LiMn_{1.5}Ni_{0.5}O_4$ is equal to that of $LiMn_{1.5}Ni_{0.45}Fe_{0.05}O_4$, the same amount of Li^+ ions was extracted from both samples at the identical SOC. Figure 5 shows the charge profiles of $LiMn_{1.5}Ni_{0.5}O_4$ and $LiMn_{1.5}Ni_{0.45}Fe_{0.05}O_4$ samples during the second charging process. The charge profile of $LiMn_{1.5}Ni_{0.45}Fe_{0.05}O_4$ presents a plateau from 4.0 to 4.3 V, which is absent from that of $LiMn_{1.5}Ni_{0.5}O_4$. This plateau is attributed to oxidation of Mn^{3+} to Mn^{4+} because the isostructural spinel $LiMn_2O_4$ exhibits a plateau in the same region. It is well known that Li ion extraction from $LiMn_2O_4$ leads to the oxidation of Mn^{3+} to Mn^{4+} [24]. The capacity of $LiMn_{1.5}Ni_{0.45}Fe_{0.05}O_4$ between the open circuit voltage (OCV) at SOC 0% and 4.3 V is 6.9 mAh/g, which is in good agreement with the theoretical capacity for the Mn^{3+} ions produced by Fe substitution to maintain electronic neutrality. It can be noted that the oxidation of Mn^{3+} to Mn^{4+} ions is completed at 4.3 V (or an SOC of 4.9%).

The DC resistance, as an indicator for the internal resistance of batteries, for $LiMn_{1.5}Ni_{0.5}O_4$ and $LiMn_{1.5}Ni_{0.45}Fe_{0.05}O_4$ was measured during the third charging process. Figure 6a, b shows the voltage drops of $LiMn_{1.5}Ni_{0.5}O_4$ and $LiMn_{1.5}Ni_{0.45}Fe_{0.05}O_4$ from OCV at SOC 60% after the momentary discharge. The absolute value of the voltage drop, which is caused by the overpotential, increased with the increase in discharge C-rate. The lower voltage drop of $LiMn_{1.5}Ni_{0.45}Fe_{0.05}O_4$ than that of $LiMn_{1.5}Ni_{0.5}O_4$ demonstrates the higher rate capability and lower internal resistance of $LiMn_{1.5}Ni_{0.45}Fe_{0.05}O_4$. Figure 6c shows the linear relationship between the discharge currents and the absolute values of the voltage drops. The DC resistances at SOC 60%, obtained from the slope of this linear relationship, were 25 Ω for $LiMn_{1.5}Ni_{0.5}O_4$ and 19 Ω for $LiMn_{1.5}Ni_{0.45}Fe_{0.05}O_4$. Figure 6d shows the DC resistances at several SOCs delivered from the same direction at SOC 60%. The resistance of $LiMn_{1.5}Ni_{0.45}Fe_{0.05}O_4$ was lower than that of $LiMn_{1.5}Ni_{0.5}O_4$ in the SOC ranges from 20 to 40% and from 60 to 90%. This decrease of DC resistance in almost all SOC ranges results in the enhancement of rate capability, as reported by Liu et al. [7]. The coexistence of Mn^{3+} and Mn^{4+} ions and the consequent increase in electronic conductivity is a well-known hypothesis for explaining the high rate capability [11]. However, this hypothesis cannot be applied for the decrease in DC resistance observed here because all the Mn^{3+} ions were consumed by oxidation to Mn^{4+} in the SOC range wherein the DC resistance was measured. The DC resistance of $LiMn_{1.5}Ni_{0.5}O_4$ at SOC 60% increased dramatically from that at SOC 50%. The DC resistance of $LiMn_{1.5}Ni_{0.45}Fe_{0.05}O_4$ at SOC 50% increased from that at SOC 40%. This behavior with increasing SOC will be considered in the following section with reference to the relationship between DC resistance and crystal structure.

To correlate the DC resistance of the samples with electrode kinetics, impedance spectroscopic analysis was conducted during the fourth charging process. Figure 7a shows typical the Nyquist plots for $LiMn_{1.5}Ni_{0.5}O_4$ and $LiMn_{1.5}Ni_{0.45}Fe_{0.05}O_4$ at SOC 60%. Both samples exhibit a single semicircle offset from the origin along the Z_{Re} axis to lower frequency and a sloped linear area in the low frequency region. The Z_{Re} axis offset is caused by

Table 2 Reliability factors, composition of phases, and lattice constant *a* values obtained from Rietveld refinement of ND data

Sample	R_{wp}	GOF	Mass fraction of phases		Lattice constant *a*	
			P4₃32	*Fd-3 m*	*P4₃32*	*Fd-3 m*
	%	–	wt%		Å	
$LiMn_{1.5}Ni_{0.5}O_4$	20.6	4.41	52	48	8.1744	8.1695
$LiMn_{1.5}Ni_{0.45}Fe_{0.05}O_4$	9.44	1.92	17	83	8.1722	8.1796

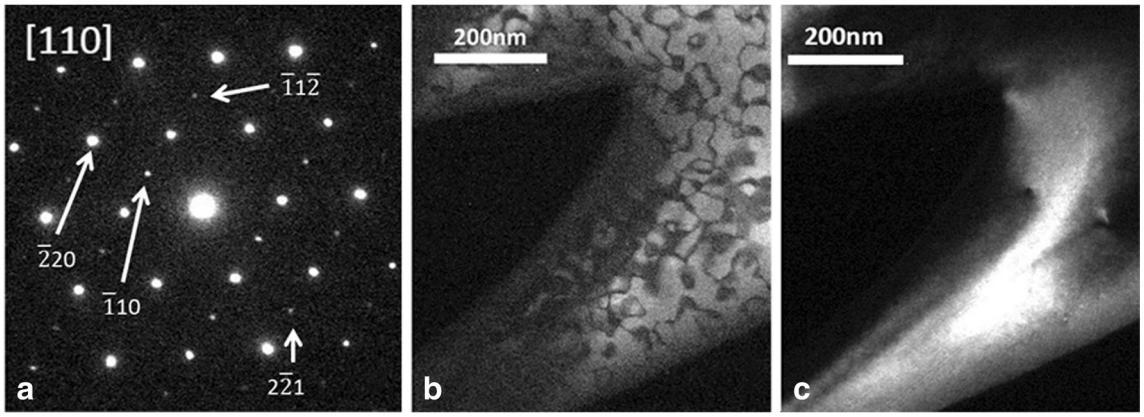

Fig. 3 The [110] zone selected area ED pattern of $LiMn_{1.5}Ni_{0.5}O_4$ (**a**) and dark-field images of the pattern of $LiMn_{1.5}Ni_{0.5}O_4$ using $\bar{1}$ 10 (**b**) and $\bar{2}$ 20 (**c**) reflections

the ohmic resistance, mainly from the electrolyte in the cell (R_{sol}). The semicircle can be fitted using a circuit model comprising a constant-phase element (CPE) and a resistor in parallel. The CPE is assigned to be double-layer capacitance. The resistor is assigned to the reaction at the interface of the electrolyte/electrode, i.e., a SEI and the charge transfer process. As reported in previous literature [25], the Nyquist plot of the lithium ion battery often has two semicircles that are assigned to the resistances from the SEI and the charge transfer process, respectively. However, the Nyquist plots in this study present one semicircle because these two resistance components have nearly the same time constants in this battery system. Thus, the resistance associated with this one semicircle is considered to be the sum of the resistances from SEI and the charge transfer process and referred to as R_{ct}. The sloped linear region indicates Warburg impedance (W) and is associated with diffusion of Li^+ ions in the solid portions of the samples. The Nyquist plots in Fig. 7a were analyzed using an equivalent circuit, as shown in Fig. 7b. This equivalent circuit is similar to the Randles circuit, which is commonly used for impedance spectroscopic analysis [26]. The respective circuit elements were determined by fitting the simulated lines to the experimental points in the Nyquist plots. The R_{sol} and R_{ct} values obtained from fitting the results at several SOCs are shown in Fig. 7c, d, respectively. The R_{sol} and R_{ct} values for $LiMn_{1.5}Ni_{0.5}O_4$ and $LiMn_{1.5}Ni_{0.45}Fe_{0.05}O_4$ were almost the same in the SOC range from 20 to 90%. The value of R_{sol} was constant irrespective of the SOC. This is reasonable because R_{sol} is determined by the type and amount of electrolyte solution used in the battery. The R_{ct} values for both samples decreased with increasing SOC. However, the R_{ct} values of both samples are almost the same at any SOC. The results indicate that the electrolyte/electrode interface does not influence the decrease of DC resistance from Fe substitution. The difference between DC resistance and the total of R_{sol} and R_{ct} ($R_{sol} + R_{ct}$) is shown in Fig. 8. The CPE component can be ignored in DC resistance; therefore, this difference in resistance is associated with the diffusion of Li^+ into the bulk of the cathode materials. The diffusion coefficient for Li^+ ions (D_{Li+}) can be estimated from Eqs. (1) and (2) [27]:

$$D_{Li+} = \frac{R^2T^2}{2A^2n^4F^4C^2\sigma^2} \tag{1}$$

$$Z_{Re} = R_{sol} + R_{ct} + \sigma\omega^{-1/2} \tag{2}$$

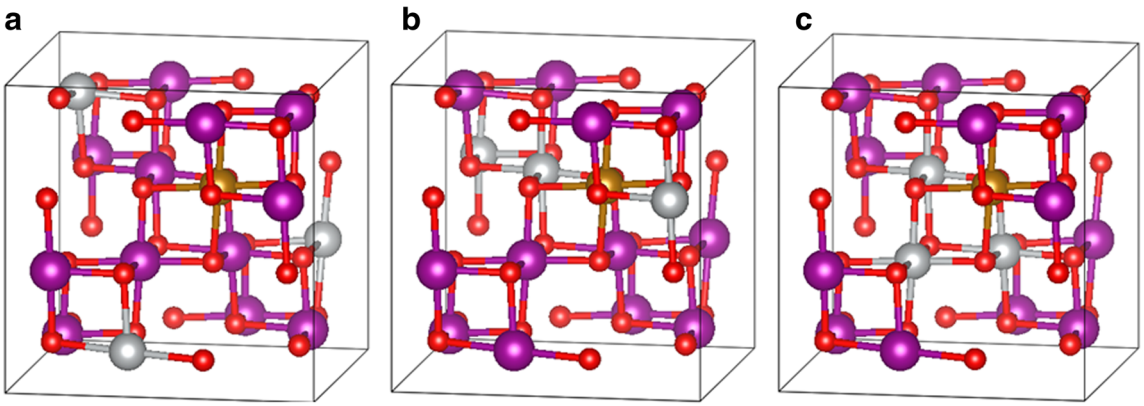

Fig. 4 Crystal structure models of $P4_332$ ordered $LiMn_{1.5}Ni_{0.5}O_4$, P model (**a**) and two variations of $Fd\bar{3}m$ disordered $LiMn_{1.5}Ni_{0.5}O_4$, A model (**b**) and B model (**c**). Li atoms are not shown to clearly demonstrate the ordering of Mn and Ni atoms. The *red*, *violet*, and *white spheres* indicate O, Mn, and Ni atoms, respectively. The *brown spheres* indicate Ni or Fe atoms

Table 3 Optimized energy of the total electrons in the crystal structure models. The values in the bracket () indicate the difference of energies between the P model and A model or B model

	Optimized energy			
	Non-substituted		Fe substituted	
	eV		eV	
P model	−355.4	–	−358.5	–
A model	−352.9	(2.5)	−357.3	(1.2)
B model	−352.8	(2.6)	−356.9	(1.6)

where R is the gas constant, T is the absolute temperature, A is the contact area of the electrode, n is the number of electrons involved in the charge transfer reaction, F is the Faraday constant, C is the concentration of Li^+ ions in the bulk of the cathode material, and σ is the Warburg coefficient associated with the slope of the linear fitting of Z_{Re} vs. the reciprocal of the square root of the angular frequency (ω) in the low frequency region from 1.0 to 0.1 Hz. A typical relationship between Z_{Re} and $\omega^{-1/2}$ is shown in Fig. 9a. T, A, n, and C are constants because the same sized cathode was used for $LiMn_{1.5}Ni_{0.5}O_4$ and $LiMn_{1.5}Ni_{0.45}Fe_{0.05}O_4$ batteries, and both samples have the same spinel-type crystal structures, electronic capacities, and BET surface areas. Therefore, σ can be used as an indicator for the reciprocal diffusion coefficient of Li^+ ions. Figure 9b shows the value of σ at several SOCs. The trend of change in the value of σ with increasing SOC is similar to that for the difference between the DC resistance and $R_{sol} + R_{ct}$ (Fig. 8). Both the values decrease from SOC 20 to 40%, increase from SOC 40 to 50% or 60%, and remain constant from 60 to 90%. These results indicate that the difference between the DC resistance and $R_{sol} + R_{ct}$ shows the Li^+ ion diffusion resistance. The decrease in DC resistance by Fe substitution is caused by the lower Li^+ ion diffusion resistance of $LiMn_{1.5}Ni_{0.45}Fe_{0.05}O_4$ than that of $LiMn_{1.5}Ni_{0.5}O_4$. These electrochemical measurements suggest that the low Li^+ ion diffusion resistance exerts its influence on the SOC in the range from 20 to 80%, which may be related to the crystal structure of the delithiated cathode materials in the batteries. The values of D_{Li+} were estimated using Eq. (1) with the σ obtained from the slope in Fig. 9a, T as 25 °C, A as the total surface area of active materials in cathode, n as 1, and C as the ratio between the tap density of the as-synthesized material, which is shown in Table 1, and the molecular weight. The D_{Li+} values at SOC 60% were 1.2×10^{-15} cm^2/s for $LiMn_{1.5}Ni_{0.5}O_4$ and 1.1×10^{-14} cm^2/s for $LiMn_{1.5}Ni_{0.45}Fe_{0.05}O_4$. The D_{Li+} value of $LiMn_{1.5}Ni_{0.5}O_4$ was consistent with previous literature [28] and lower than that of conventional cathode active materials such as $LiCoO_2$, $LiNiO_2$, and $LiMn_2O_4$ (from 10^{-11} to 10^{-7}) [29–32]. Thus, the increased Li^+ ion diffusion coefficient of cathode active material significantly improved the total internal resistance of the battery when using the $LiMn_{1.5}Ni_{0.5}O_4$ cathode.

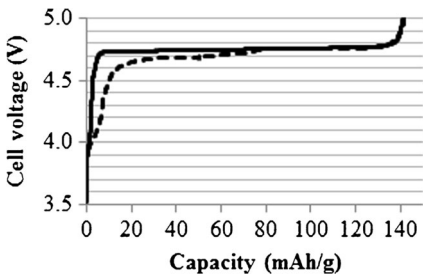

Fig. 5 Charge profiles of $LiMn_{1.5}Ni_{0.5}O_4$ (*solid line*) and $LiMn_{1.5}Ni_{0.45}Fe_{0.05}O_4$ (*dashed line*)

As described above, a number of studies have reported the improvement of cycle durability after Fe substitution [6, 7]. Figure 10 shows the cycling performances of $LiMn_{1.5}Ni_{0.5}O_4$ and $LiMn_{1.5}Ni_{0.45}Fe_{0.05}O_4$. Both samples have the almost same initial discharge capacities (116 mAh/g). The discharge capacity after 200 cycles was 63.7 mAh/g (55% of the initial capacity) for $LiMn_{1.5}Ni_{0.5}O_4$ and 75.2 mAh/g (65% of the initial capacity) for $LiMn_{1.5}Ni_{0.45}Fe_{0.05}O_4$. As in the case with previous literature [6, 7], the $LiMn_{1.5}Ni_{0.45}Fe_{0.05}O_4$ synthesized in this study also exhibited a higher cycle durability than that of $LiMn_{1.5}Ni_{0.5}O_4$. It has been known that the TM dissolution from $LiMn_{1.5}Ni_{0.5}O_4$ causes capacity fading in a cycling test [33]. The amount of Mn and Ni on the carbon composite anodes after the cycling tests was measured using ICP. The anode against the $LiMn_{1.5}Ni_{0.5}O_4$ cathode contained a higher amount of Mn and Ni (230 μg for Mn and 60 μg for Ni) than that against $LiMn_{1.5}Ni_{0.45}Fe_{0.05}O_4$ (130 μg for Mn and 17 μg for Ni). Fe substitution suppressed the dissolution of Mn and Ni ions, although the reason for this suppression is unclear.

Crystal structure of the delithiated samples

To investigate the relationship between resistance and crystal structure, in situ XRD measurements were performed during the third charging process. Figure 11a shows the XRD patterns of $LiMn_{1.5}Ni_{0.5}O_4$ at several SOCs. The angle region around the (311) peak of the as-synthesized $LiMn_{1.5}Ni_{0.5}O_4$ is magnified in Fig. 11a. Peaks attributed to three different cubic phases appear depending on the SOC. These peaks indicate that the delithiated $LiMn_{1.5}Ni_{0.5}O_4$ in the cathode contained both the pristine cubic phase (MN-1) and a secondary cubic phase (MN-2) in the SOC range from 0 to 50% and also contained MN-2 and a third cubic phase (MN-3) in the SOC range from 50 to 100%. This type of crystal structure variation wherein separation into more than two phases on account of Li^+ ion extraction occurs is termed a multi-phase

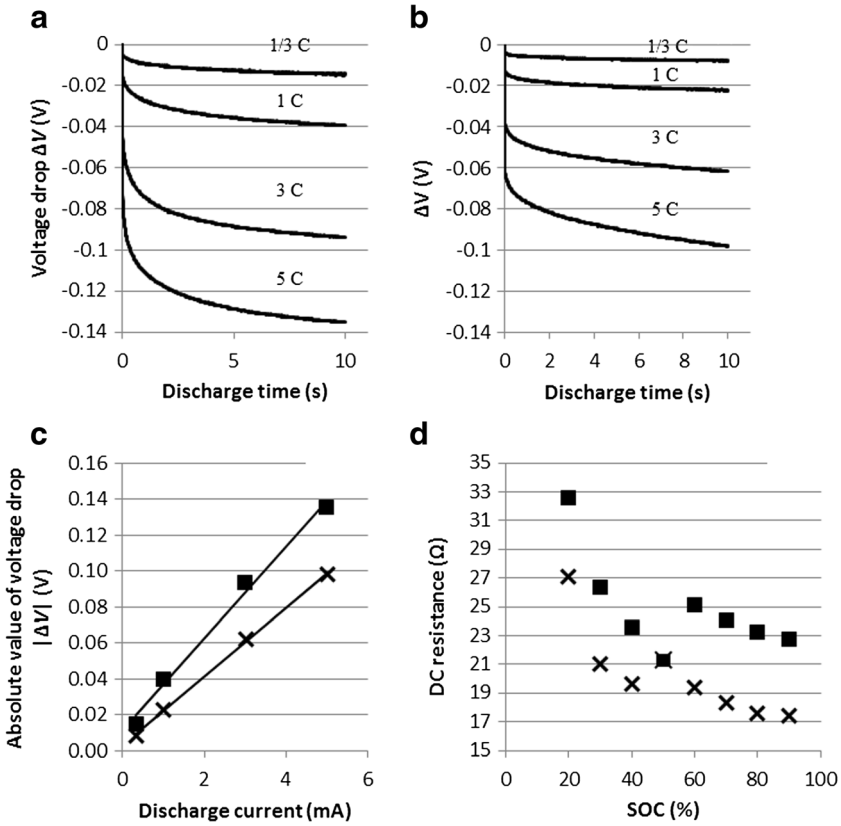

Fig. 6 Voltage drops (ΔV) of $LiMn_{1.5}Ni_{0.5}O_4$ (**a**) and $LiMn_{1.5}Ni_{0.45}Fe_{0.05}O_4$ (**b**) from OCV at SOC 60% with several constant current discharges for 10 s. Linear relationship between the discharge currents and the absolute values of voltage drops at SOC 60% (**c**). DC resistance at several SOC (**d**). $LiMn_{1.5}Ni_{0.5}O_4$ (*black square*) and $LiMn_{1.5}Ni_{0.45}Fe_{0.05}O_4$ (*multiplication sign*)

reaction. Figure 11b shows the crystal structure variation for $LiMn_{1.5}Ni_{0.45}Fe_{0.05}O_4$ in which the three different cubic phases are also observed. The peaks attributed to the pristine cubic phase (Fe05–1) and secondary cubic phase (Fe05–2) in the XRD patterns of the delithiated $LiMn_{1.5}Ni_{0.45}Fe_{0.05}O_4$ shifted to higher angles with increasing SOC and did not separate, unlike those for $LiMn_{1.5}Ni_{0.5}O_4$ in the SOC range from 20 to 30%. A third cubic phase (Fe05-3) appeared at SOC 60%. Phase separation of Fe05-2 and Fe05-3 was observed clearly in the SOC range from 60 to 90%, as with $LiMn_{1.5}Ni_{0.5}O_4$. The crystal structure variations of the samples are summarized in Fig. 11c, which shows the lattice constant a at several SOC values. Since the lattice constants were calculated from the 2θ positions of the (311) peaks, the absolute value of the lattice constants is not accurate. However, the lattice constants provide sufficient information on the

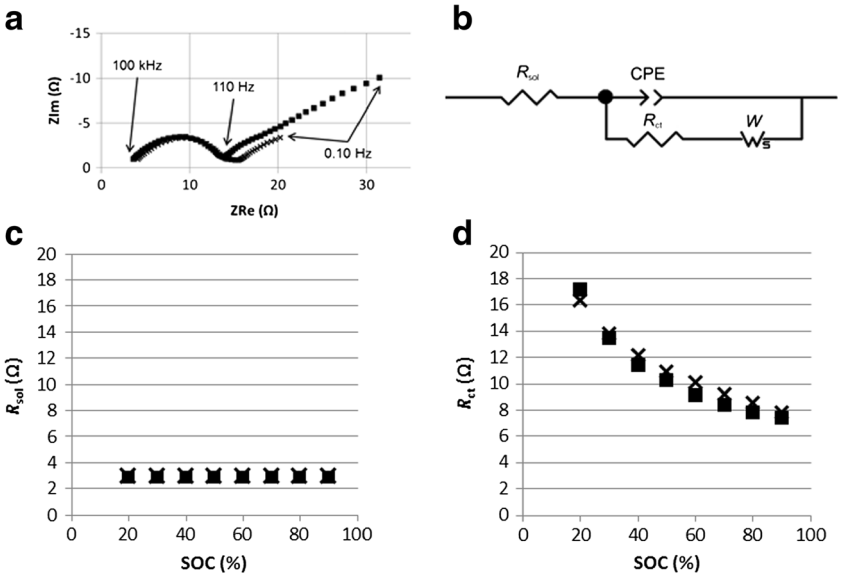

Fig. 7 Nyquist plots at SOC 60% (**a**), equivalent circuit model (**b**), R_{sol} (**c**), and R_{ct} (**d**) at several SOC. $LiMn_{1.5}Ni_{0.5}O_4$ (*black square*) and $LiMn_{1.5}Ni_{0.45}Fe_{0.05}O_4$ (*multiplication sign*)

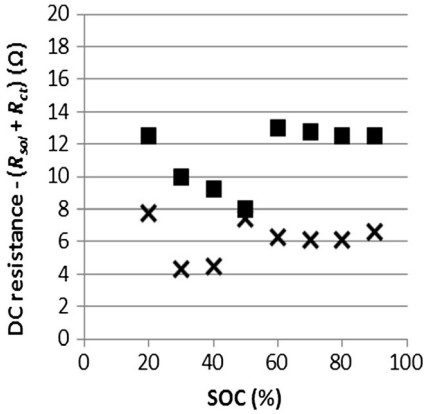

Fig. 8 DC resistance − (R_{sol} + R_{ct}) at several SOC of $LiMn_{1.5}Ni_{0.5}O_4$ (*black square*) and $LiMn_{1.5}Ni_{0.45}Fe_{0.05}O_4$ (*multiplication sign*)

tendency of the crystal structure variations. The lattice constant of MN-1 at SOC 0% was smaller than that of Fe05-1. This difference is consistent with the ND data for the $Fd\bar{3}m$ phases in the as-synthesized samples. As described above, a higher Mn^{3+} ions content increases the lattice constant of the as-synthesized structures. The lattice constants of MN-1 and Fe05-1 at SOC 10% are almost the same. This similarity indicates that Mn^{3+} ions do not exist in both samples at SOC 10% or over. This result is in accordance with the charge profiles (Fig. 5), which reveal that the oxidation of Mn^{3+} to Mn^{4+} ions is complete by SOC 4.9%. The Mn^{3+} ions affect the crystal structure or electronic conductivity of the as-synthesized samples, as reported by Kunduraci et al. [11]. However, the Mn^{3+} ions did not affect the internal resistance at SOC 20% or over because they disappeared. In the SOC range from 50 to 60%, the cathode materials exhibited a single phase such as Mn-2 and Fe05-2. Although the physical meaning of the Warburg coefficient or the Li^+ ion diffusion coefficient is uncertain in multi-phase reactions, both samples at SOC 50% had higher Warburg coefficients than those at SOC 40%. This is because the intermediate single phase in the multi-phase reaction is thermodynamically stable, making it difficult to insert or extract Li^+ ions. $LiMn_{1.5}Ni_{0.5}O_4$ and $LiMn_{1.5}Ni_{0.45}Fe_{0.05}O_4$ exhibited similar phase separations in the SOC range from 60 to 80%, although the DC resistances of $LiMn_{1.5}Ni_{0.5}O_4$ in the same SOC range were still larger than those of $LiMn_{1.5}Ni_{0.45}Fe_{0.05}O_4$. This result indicates that phase separation or inhomogeneous Li^+ ion extraction was not the direct causes of the increased internal resistance in batteries. The phase separation induces internal stress on the primary particles because there is a large mismatch of the lattice constants between the separated phases. This internal stress will lead to the dissolution of Mn and Ni ions, which causes capacity fading in the cycling test. The incomplete multi-phase reaction of $LiMn_{1.5}Ni_{0.45}Fe_{0.05}O_4$ in the SOC range from 20 to 40% is probably associated with the improvement of the cycle durability from Fe substitution. Yavuz et al. reported that the $Li_xNi_{1-x}O$ impurity phase lead to the multi-phase reaction [34]. However, the amount of impurity phase in $LiMn_{1.5}Ni_{0.5}O_4$ (0.64 wt%) obtained from Rietveld refinement for XRD patterns was equal to that in $LiMn_{1.5}Ni_{0.45}Fe_{0.05}O_4$ (0.48 wt%). Thus, the small amount of the impurity phase does not affect the difference of the cycle durability or electrochemical reaction mechanism between $LiMn_{1.5}Ni_{0.5}O_4$ and $LiMn_{1.5}Ni_{0.45}Fe_{0.05}O_4$.

The XRD data did not provide information regarding the ordering of the Mn and Ni ions. However, the major difference between $LiMn_{1.5}Ni_{0.5}O_4$ and $LiMn_{1.5}Ni_{0.45}Fe_{0.05}O_4$ was in the amount of $P4_332$ ordered phase in the as-synthesized structures. To obtain information about the ordering of the Mn and Ni ions in the delithiated samples, ex situ ND was performed. Figure 12a–d shows the ND diffraction patterns of $LiMn_{1.5}Ni_{0.5}O_4$ and $LiMn_{1.5}Ni_{0.45}Fe_{0.05}O_4$ at SOCs of 0, 40, and 80% during the third charging process. The ND patterns of the samples at SOC 0% were similar to those of the as-

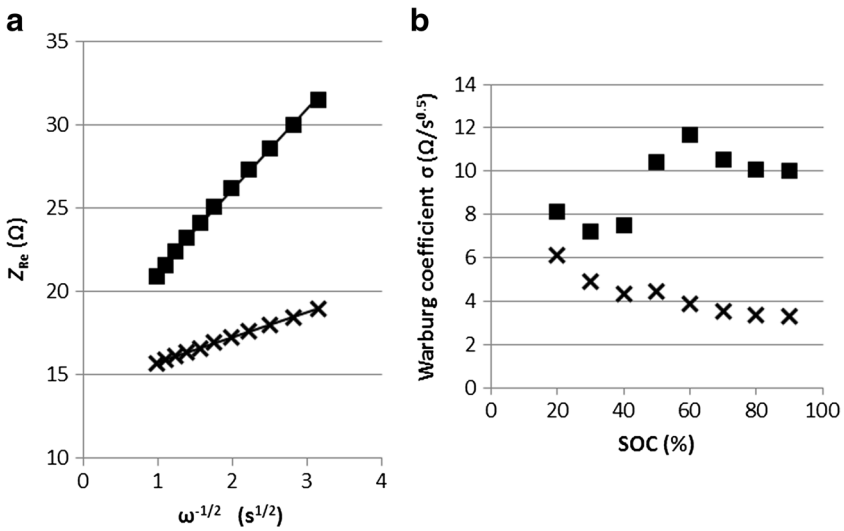

Fig. 9 Relationship between Z_{Re} and $\omega^{-1/2}$ in the low frequency region from 1.0 to 0.1 Hz at SOC 60% (**a**) and Warburg coefficient σ at several SOC (**b**). $LiMn_{1.5}Ni_{0.5}O_4$ (*black square*) and $LiMn_{1.5}Ni_{0.45}Fe_{0.05}O_4$ (*multiplication sign*)

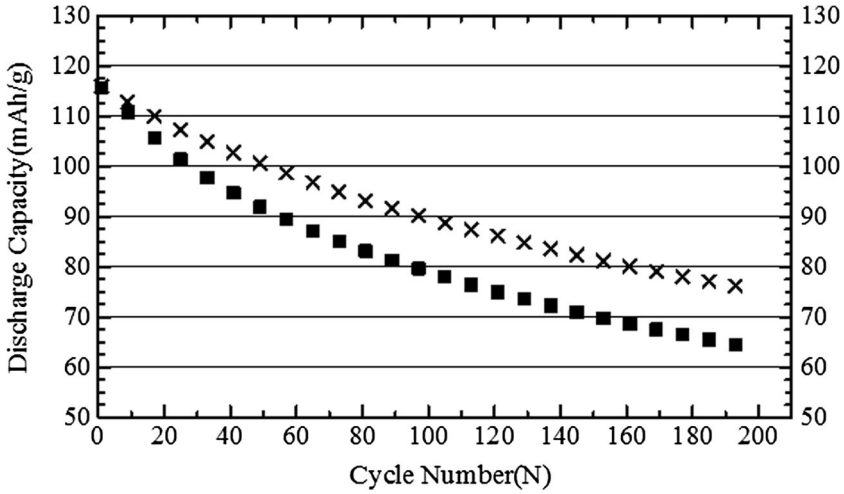

Fig. 10 Cycle durability of the $LiMn_{1.5}Ni_{0.5}O_4$ (*black square*) and $LiMn_{1.5}Ni_{0.45}Fe_{0.05}O_4$ (*multiplication sign*) at 25 °C with a carbon composite anode

synthesized structure and exhibit the two types of peaks, i.e., P peaks and F peaks, as shown in Fig. 2. The ND patterns show that the $P4_332$ phase existed after two charge/discharge cycles. The F peaks (unmarked) of both samples indicate the multi-phase reaction, as observed with in situ XRD (Fig. 11). The similar in situ XRD and ex situ ND results indicated that

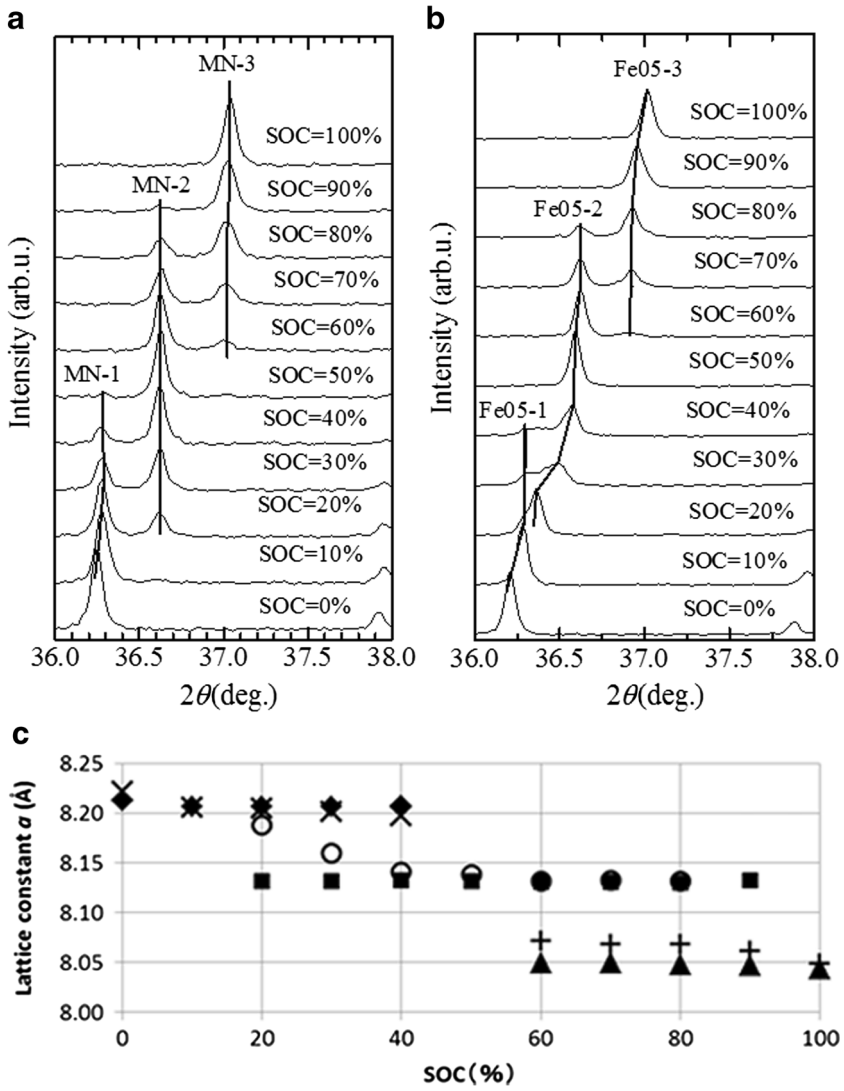

Fig. 11 In situ XRD patterns of $LiMn_{1.5}Ni_{0.5}O_4$ (**a**) and $LiMn_{1.5}Ni_{0.45}Fe_{0.05}O_4$ (**b**). Lattice constants at several SOC (**c**). MN-1 (*black diamond sign*), MN-2 (*black square sign*), MN-3 (*black triangle sign*), Fe05-1(*multiplication sign*), Fe05-2(*white circle sign*) and Fe05-3(*plus sign*)

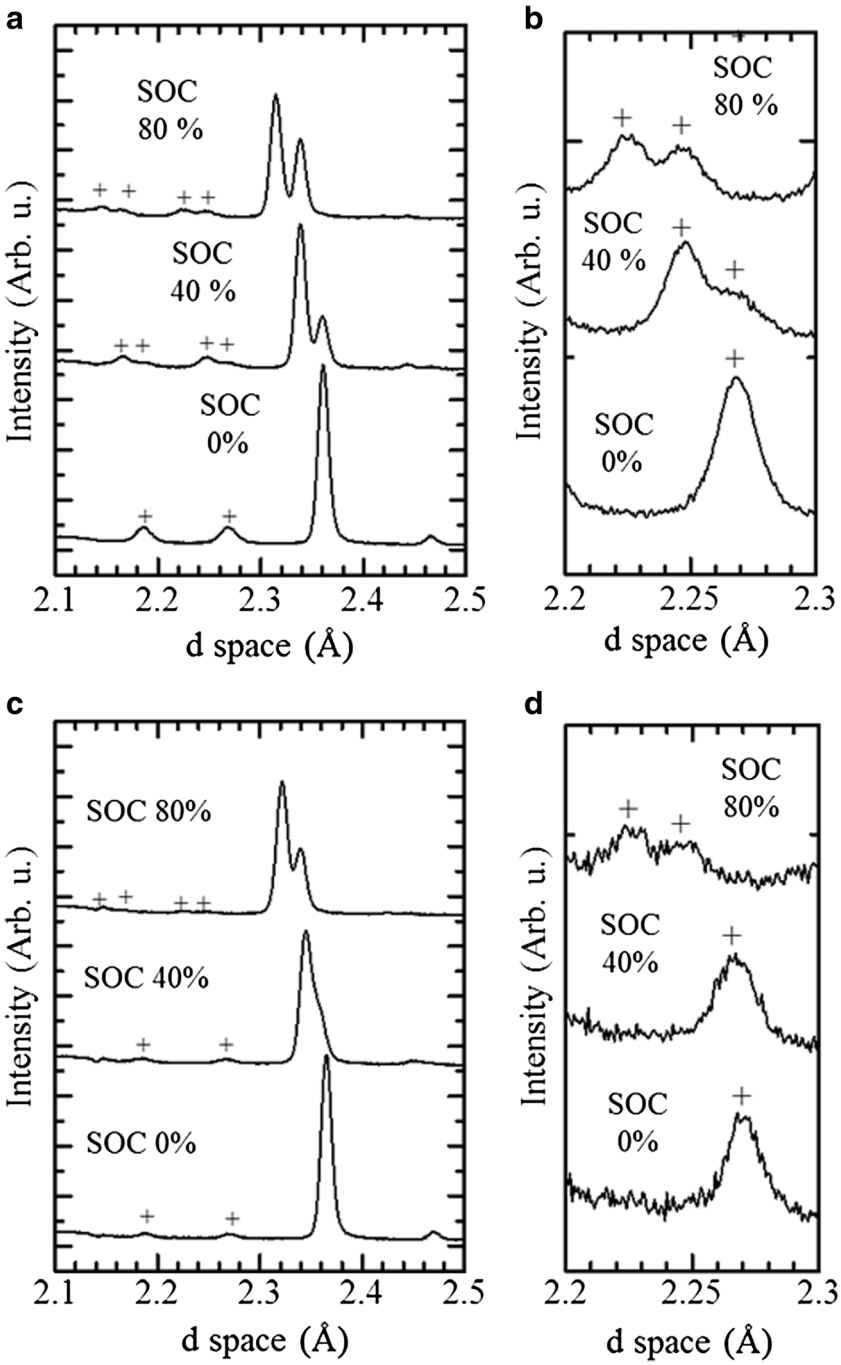

Fig. 12 Ex situ ND patterns of $LiMn_{1.5}Ni_{0.5}O_4$ (**a**, **b**) and $LiMn_{1.5}Ni_{0.45}Fe_{0.05}O_4$ (**c**, **d**). *The peaks with plus sign mark* indicate P peaks. *The peaks without marks* indicate F peaks

the crystal structures of the cathode materials in the batteries during operation were virtually the same as those in the electrodes retrieved from the disassembled batteries. The P peaks (with the + mark) can be observed at SOC 40 and 80%, and they also indicate a multi-phase reaction. Rietveld refinement was performed to determine the quantities of all the phases in the samples. Figure 13a shows the mass fraction of the phases in $LiMn_{1.5}Ni_{0.5}O_4$ at several SOCs. The mass percentage of the $P4_332$ phase at SOC 0% (64 wt%) was larger than that in the as-synthesized sample, as shown in Table 2 (52 wt%). This increase in the mass percentage of the $P4_332$ phase can be ascribed to the error due to the difference between the powder and electrode samples, such as the influence of background from the conductive binder in the electrode. Thus, only the results of Rietveld refinement for ex situ ND may be compared meaningfully. The total mass fraction of the $P4_332$ phase in $LiMn_{1.5}Ni_{0.5}O_4$ decreased with increasing SOC (the total heights of the black bar without patterning and those with cross and grid patterns in Fig. 13a). This decrease indicated the migration of Mn and Ni ions and the consequent structural

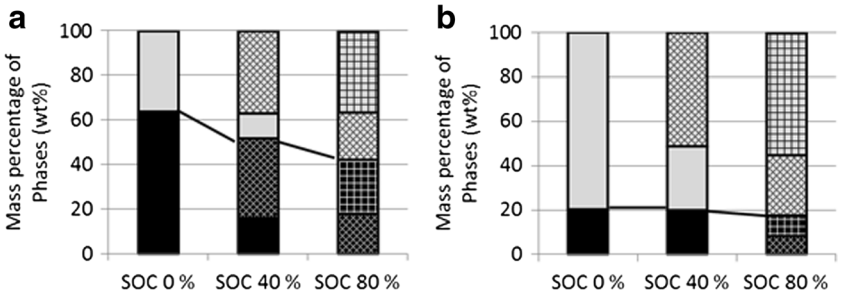

Fig. 13 Mass fraction of the phases at several SOC of the $LiMn_{1.5}Ni_{0.5}O_4$ (**a**) and $LiMn_{1.5}Ni_{0.45}Fe_{0.05}O_4$ (**b**). The *black bars* indicate the $P4_332$ phase. The *gray bars* indicate the $Fd\bar{3}$ m phase. *The bars without patterns* indicate the MN-1 or Fe05-1 phase. *The bars with a cross pattern* indicate the MN-2 or Fe05-2 phase. *The bars with a grid pattern* indicate the MN-3 or Fe05-3 phase

transformation from the $P4_332$ phase to the $Fd\bar{3}m$ phase. Figure 13b shows the mass fractions of the phases in $LiMn_{1.5}Ni_{0.45}Fe_{0.05}O_4$ at several SOCs. The mass percentage of the $P4_332$ phase remained constant in the range from SOC 0% to 80% (the total heights of the black bar without patterning and those with cross and grid patterns in Fig. 13b). As reported by Kim et al., their ED data showed that 50% extraction of Li^+ ions from $P4_332$ phase $LiMn_{1.5}Ni_{0.5}O_4$ led to the complete disordering of the Ni and Mn ions with a concurrent structural transformation to the $Fd\bar{3}m$ phase [9]. They also reported that the $Fd\bar{3}m$ phase observed in $LiMn_{1.5}Ni_{0.5}O_4$ at SOC 50% corresponds to the intermediate secondary cubic phase observed in the ex situ XRD pattern (denoted by MN-2 in the present paper) [9, 10]. Based on these reports, Liu et al. concluded that stabilization of structures with the $Fd\bar{3}m$ space group from Fe substitution suppresses the phase separation upon multi-phase reaction and improves the rate capability [7]. However, the ex situ ND data in the present study are inconsistent with the hypotheses presented in those previous reports. The ex situ ND data indicate that inhomogeneous Li^+ ion extraction is independent of the phase transition from the $P4_332$ phase to the $Fd\bar{3}m$ phase. Furthermore, according to the above in situ XRD data, phase separation upon multi-phase reaction is not a direct cause of increased internal resistance in batteries. However, the argument that Fe substitution suppresses the migration of Mn and Ni ions and decreases the internal resistance of batteries seems to be correct. If the migration of Mn and Ni ions along with Li ions is required in the charge/discharge process, extra energy will be required to move the Mn and Ni ions, and this will be reflected by an apparent increase in Li^+ ion diffusion resistance.

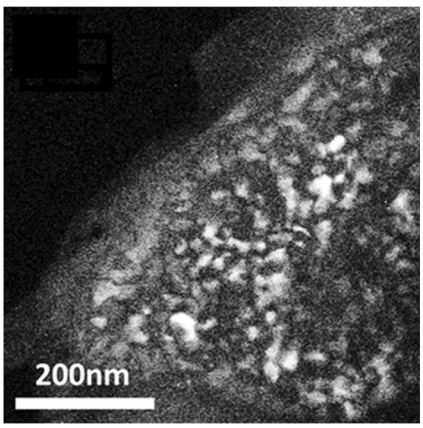

Fig. 14 Dark-field images of the $LiMn_{1.5}Ni_{0.5}O_4$ intermediates at SOC 40% using reflections attributed to the $P4_332$ ordered phase

TEM was performed to observe the distribution of $P4_332$ phases in the primary particles of delithiated $LiMn_{1.5}Ni_{0.5}O_4$ at SOC 40% and SOC 80% during the third charging process. Extra spots due to the $P4_332$ phase were not observed in the ED patterns of $LiMn_{1.5}Ni_{0.5}O_4$ at SOC 80%. As has been reported by *Kim* et al. [9], it was difficult to detect the $P4_332$ phase by ED measurement in samples at SOC 60% or over, although our ND data prove the existence of a $P4_332$ phase in lithiated $LiMn_{1.5}Ni_{0.5}O_4$. The reason for this discrepancy is due to differences in the specimen regions, as described in the section dealing with TEM observation of the as-synthesized samples. ND is supposed to be the most reliable way to confirm the existence of $P4_332$ phases in a sample. Figure 14 shows the dark-field images of delithiated $LiMn_{1.5}Ni_{0.5}O_4$ at SOC 40%. These images were captured in a similar manner as those shown in Fig. 3b. The domains in the primary particles due to the ordering of the Mn and Ni ions can be observed in Fig. 14. As observed in Fig. 3b, the bright domains and dark domains indicate the ordered $P4_332$ phase and the disordered $Fd\bar{3}m$ phase, respectively. This domain structure should exist in the delithiated $LiMn_{1.5}Ni_{0.5}O_4$ and $LiMn_{1.5}Ni_{0.45}Fe_{0.05}O_4$ in the range from SOC 0% to SOC 80% because the ex situ ND data indicate the existence of $P4_332$ phases, as shown in Fig. 13. The domain structure implies that the boundary between the domains impedes the diffusion of Li^+ ions because there is a local distortion between the two different crystal phases. The low Li^+ ion diffusion resistance of $LiMn_{1.5}Ni_{0.45}Fe_{0.05}O_4$ was probably caused by the smaller number of boundaries between the crystal structures. This inference is consistent with the fact that $LiMn_{1.5}Ni_{0.45}Fe_{0.05}O_4$ maintains a lower Li^+ ion diffusion resistance than $LiMn_{1.5}Ni_{0.5}O_4$ over the wide SOC range from

20 to 90% because the amount of $P4_332$ phase in the as-synthesized structure controls the number of boundaries in the entire SOC range. Based on the above consideration, the stabilization of the structure with the $Fd\bar{3}m$ space group is the most important cause of the improvement in Li^+ ion diffusion resistance for $LiMn_{1.5}Ni_{0.5}O_4$ upon Fe substitution.

Conclusions

$LiMn_{1.5}Ni_{0.5}O_4$ and $LiMn_{1.5}Ni_{0.45}Fe_{0.05}O_4$ samples were synthesized and their crystal structures and electrochemical performances were comparatively studied to understand the mechanism for the rate capability improvement previously reported [7]. The electrochemical measurements showed that $LiMn_{1.5}Ni_{0.5}O_4$ exhibited a higher internal resistance than $LiMn_{1.5}Ni_{0.45}Fe_{0.05}O_4$ because the latter exhibited lower resistance to the diffusion of Li^+ ions into the bulk of the cathode materials. ND data indicated that both samples contained the ordered $P4_332$ phase and the disordered $Fd\bar{3}m$ phase. The mass percentage of the $P4_332$ phase in $LiMn_{1.5}Ni_{0.45}Fe_{0.05}O_4$ (17 wt%) was smaller than that in $LiMn_{1.5}Ni_{0.5}O_4$ (52 wt%) because Fe substitution stabilized the disordered $Fd\bar{3}m$ phase. TEM observations with dark-field images demonstrated that the coexistence of two different crystal structures in the same sample leads to the primary particles separating into discrete domains of $P4_332$ and $Fd\bar{3}m$ phases. The boundaries between the domains possibly impede the diffusion of Li^+ ions because of local distortions between the two different crystal phases. Ex situ ND proved that the $P4_332$ phase remained at SOC 80% during the third charge process. It was expected that boundaries existed in the delithiated samples. Moreover, the boundaries could be observed in $LiMn_{1.5}Ni_{0.5}O_4$ at SOC 40%. $LiMn_{1.5}Ni_{0.45}Fe_{0.05}O_4$ exhibited low internal resistance because it contained less $P4_332$ phases and, therefore, few boundaries between $P4_332$ and $Fd\bar{3}m$ phases. Work will be undertaken in the future to prove that the boundaries of cation ordering/disordering will result in a higher resistance. The ab initio calculation approach will be used to demonstrate the high activation energy required for diffusion of Li^+ ions at the boundary.

Acknowledgments The authors are grateful to Dr. T. Ishigaki and Dr. Y. Yoshida from the Frontier Research Center for Applied Atomic Sciences, Ibaraki University, Japan, for their detailed instruction on neutron diffraction.

References

1. Sigala C, Verbaere A, Mansot JL, Guyomard D, Piffard Y, Tournoux M (1997) The Cr-substituted spinel Mn oxides LiCryMn2−yO4(0≤y≤1): Rietveld analysis of the structure modifications induced by the electrochemical lithium deintercalation. J Solid State Chem 132:372–381
2. Kawai H, Nagata M, Tabuchi M, Tukamoto H, West AR (1998) Novel 5 V spinel cathode Li2FeMn3O8 for lithium ion batteries. Chem Mater 10:3266–3268
3. Kawai H, Nagata M, Tukamoto H, West AR (1998) A new lithium cathode LiCoMnO4: toward practical 5 V lithium batteries. Electrochem Solid-State Lett 1:212–214
4. Zhong Q, Bonakdarpour A, Zhanga M, Gao Y, Dahn JR (1997) Synthesis and electrochemistry of $LiNi_xMn_{2-x}O_4$. J Electrochem Soc 144:205–213
5. Ein-Eli Y, Howard WF Jr, Lu SH, Mukerjee S, McBreen J, Vaughey JT, Thackeray MM (1998) $LiMn_{2-x}Cu_xO_4$ Spinels ($0.1 \leqslant \times \leqslant 0.5$): a new class of 5 V cathode I. Electrochemical, structural, and spectroscopic studies materials for Li batteries. J Electrochem Soc 145: 1238–1244
6. Alcántara R, Jaraba M, Lavela P, Lloris JM, Pérez Vicente C, Tirado C (2005) Synergistic effects of double substitution in $LiNi_{0.5-y}Fe_yMn_{1.5}O_4$ spinel as 5 V cathode materials. J Electrochem Soc 152:A13–A18
7. Liu J, Manthiram A (2009) Understanding the improved electrochemical performances of Fe-substituted 5 V spinel cathode $LiMn_{1.5}Ni_{0.5}O_4$. J Phys Chem C 113:15073–15079
8. Gryffroy D, Vandenberghe RE (1992) Cation distribution, cluster structure and ionic ordering of the spinel series $LiNi_{0.5}Mn_{1.5-x}Ti_xO_4$ and $LiNi_{0.5-y}Mg_yMn_{1.5}O_4$. J Phys Chem Solids 53:777–784
9. Kim JH, Myung ST, Yoon CS, Kang SG, Sun YK (2004) Comparative study of $LiNi_{0.5}Mn_{1.5}O_{4-\delta}$ and $LiNi_{0.5}Mn_{1.5}O_4$ cathodes having two crystallographic structures: Fd$\bar{3}$m and P4332. Chem Mater 16:906–914
10. Kim JH, Myung ST, Yoon CS, Oh IH, Sun YK (2004) Effect of Ti substitution for Mn on the structure of $LiNi_{0.5}Mn_{1.5-x}Ti_xO_4$ and their electrochemical properties as lithium insertion material. J Electrochem Soc 151:A1911–A1918
11. Kunduraci M, Al-Sharab JF, Amatucci GG (2006) High-power nanostructured $LiMn_{2-x}Ni_xO_4$ high-voltage lithium ion battery electrode materials: electrochemical impact of electronic conductivity and morphology. Chem Mater 18:3585–3592
12. Hohenberg P, Kohn W (1964) Inhomogeneous electron gas. Phys Rev 136:B864–B870
13. Kresse G, Furthmüller J (1996) Efficient iterative schemes for ab initio total-energy calculations using a plane-wave basis set. Phys Rev B 54:11169–11186
14. Kresse G, Furthmüller J (1996) Efficiency of ab-initio total energy calculations for metals and semiconductors using a plane-wave basis set. Comput Mater Sci 6:15–50
15. Kresse G, Hafner J (1993) Ab initio molecular dynamics for liquid metals. Phys Rev B 47:558–561
16. Kresse G, Joubert D (1997) From ultrasoft pseudopotentials to the projector augmented-wave method. Phys Rev B 59:1758–1775
17. Perdew JP, Burke K, Ernzerhof M (1996) Generalized gradient approximation made simple. Phys Rev Lett 78:3865–3868
18. Perdew JP, Wang Y (1992) Accurate and simple analytic representation of the electron-gas correlation energy. Phys Rev B 45:13244–13249
19. Blöchl PE (1994) Projector augmented-wave method. Phys Rev B 50:17953–17979
20. Liechtenstein AI, Anisimov VI, Zaanen J (1995) Density-functional theory and strong interactions: orbital ordering in Mott-Hubbard insulators. Phys Rev B 52:R5467–R5470
21. Gryffroy D, Vandenberghe RE, Legrand E (1991) A neutron diffraction study of some spinel compounds containing octahedral Ni and Mn at a 1:3 ratio. Mater Sci Forum 79–82:785–790
22. Pasero D, Reeves N, Pralong V, West AR (2008) Oxygen nonstoichiometry and phase transitions in $LiMn_{1.5}Ni_{0.5}O_{4-\delta}$. J Electrochem Soc 155:A282–A291
23. Shin DW, Bridges CA, Huq A, Paranthaman MP, Manthiram A (2012) Role of cation ordering and surface segregation in high-

voltage spinel $LiMn_{1.5}Ni_{0.5-x}M_xO_4$ (M = Cr, Fe, and Ga) cathodes for lithium ion batteries. Chem Mater 24:3720–3731
24. Shiraishi Y, Nakai I, Tsubata T, Himeda T, Nishikawa F (1997) In situ transmission X-ray absorption fine structure analysis of the charge–discharge process in $LiMn_2O_4$, a rechargeable lithium battery material. J Solid State Chem 133:587–590
25. Liu J, Manthiram A (2009) Understanding the improvement in the electrochemical properties of surface modified 5 V $LiMn_{1.42}Ni_{0.42}Co_{0.16}O_4$ spinel cathodes in lithium-ion cells. Chem Mater 21:1695–1707
26. Randles JEB (1947) Kinetics of rapid electrode reactions. Discuss Faraday Soc 1:11–19
27. Bard AJ, Faulkner LR (2001) In: (ed) Electrochemical methods, 2nd edn. Wiley, New York
28. Yi TF, Fang ZK, Xie Y, Zhu YR, Zang LY (2014) Synthesis of $LiNi_{0.5}Mn_{1.5}O_4$ cathode with excellent fast charge-discharge performance for lithium ion battery. Electrochim Acta 147:250–256
29. Honders A, der Kinderen JM, van Heeren AH, Wit JHW, Broers GHJ (1985) Bounded diffusion in solid solution electrode powder compacts. Part II. The simultaneous measurement of the chemical diffusion coefficient and the thermodynamic factor in Li_xTiS_2 and Li_xCoO_2. Solid State Ionics 15:265–276
30. Bruce PG, Lisowska-Oleksiak A, Saidi MY, Vincent CA (1992) Vacancy diffusion in the intercalation electrode $Li_{1-x}NiO_2$. Solid State Ionics 57:353–358
31. Thomas MGSR, Bruce PG, Goodenough JB (1986) AC impedance of the $Li_{1-x}CoO_2$ electrode. Solid State Ionics 18–19:794–798
32. Dokko K, Mohamedi M, Umeda M, Uchida I (2003) Kinetic study of li-ion extraction and insertion at $LiMn_2O_4$ single particle electrodes using potential step and impedance methods. J Electrochem Soc 150:A425–A429
33. Kim JH, Pieczonka NPW, Li Z, Wu Y, Harris S, Powell BR (2013) Understanding the capacity fading mechanism in $LiNi_{0.5}Mn_{1.5}O_4$/graphite Li-ion batteries. Electrochim Acta 90:556–562
34. Yavuz M, Kiziltas-Yavuz N, Bhaskar A, Scheuermann M, Indris S, Fauth F, Knapp M, Ehrenberg H (2014) Influence of iron on the structural evolution of $LiNi_{0.4}Fe_{0.2}Mn_{1.4}O_4$ during electrochemical cycling investigated by in situ powder diffraction and spectroscopic methods. Z Anorg Allg Chem 640:3118–3126